Hybrid quantum lattice model: Polaritons, photons, and spin waves propagation

M. Ahumada ,[1,*] N. Valderrama-Quinteros ,[1] D. Tancara ,[1] and G. Romero [2,†]

[1] *Departamento de Física, Universidad de Santiago de Chile (USACH), Avenida Víctor Jara 3493, 9170124, Santiago, Chile*

[2] *Departamento de Física, CEDENNA, Universidad de Santiago de Chile (USACH), Avenida Víctor Jara 3493, 9170124, Santiago, Chile*

Controlling the propagation of quantum excitations in low-dimensional systems is pivotal for advancing quantum technologies, including communication networks and quantum simulators. We propose a one-dimensional hybrid quantum lattice model comprising coupled cavity quantum electrodynamics (QED) units. Each unit integrates a single-mode cavity that interacts with a two-level system (TLS), featuring direct coupling between adjacent TLSs. This configuration enables the coherent propagation of polaritons, spin waves, and photons, depending on the interplay between light–matter coupling and spin–spin interactions. Employing the time-evolving block decimation (TEBD) algorithm, we simulate the dynamics of various excitation configurations and analyze their transport characteristics using local observables. Our analysis reveals the importance of matching impedance and resonance conditions via system parameters for the propagation of different types of excitations or swapping the nature of excitations along the hybrid lattice. These findings offer insights into designing controllable quantum links and single-excitation swaps in low-dimensional quantum systems.

arXiv:2507.12319v1 [quant-ph] 16 Jul 2025

I. INTRODUCTION

The precise control of excitation propagation in quantum systems is a fundamental requirement for quantum communication networks [1, 2], quantum simulators [3, 4], energy transfer devices [5, 6], quantum state transfer [7–18], and distributed quantum computing [19–25]. In particular, one-dimensional (1D) quantum lattices provide an ideal platform for exploring the dynamics of different excitation types, including photons, polaritons, and spin waves. Advancements in cavity QED [26, 27], spin chain systems [28], trapped ions [29, 30], and superconducting circuits [31–33] have enabled the realization of hybrid models where light–matter interactions and spin–spin couplings can be engineered to tailor excitation dynamics.

A scenario where different types of excitations appear is the Jaynes-Cummings-Hubbard (JCH) model [34–36], a paradigmatic model for studying quantum phase transitions. Their static and dynamical properties have been a subject of great interest [37–51]. Recently, the JCH model has been proposed for quantum state transfer in short-range communication lattice [52, 53]. One may wonder what other scenarios, physically implementable in quantum simulators [3, 4], may also support the propagation of different types of excitations on-chip.

This work addresses the previous concern, proposing a 1D hybrid quantum lattice model comprising coupled cavity-QED units. This configuration enables the propagation of distinct excitation types: polaritons, spin waves, and photons. Additionally, the proposed model enables the swapping of excitations based on the relative strengths of the light–matter coupling and spin–spin interactions. By tuning these parameters, we focus on controlling the transport properties of each excitation type within a unified framework.

To analyze the dynamics of this system, we employ the time-evolving block decimation (TEBD) algorithm [54–56], which allows efficient simulation of nonequilibrium many-body systems. Our simulations reveal transport characteristics for each excitation type and highlight the role of system parameters in modulating propagation behavior. These results provide a foundation for designing controllable quantum links [17, 18, 57] and single-excitation swapping, with potential applications in quantum information processing, energy transfer, and the simulation of strongly correlated light–matter systems.

II. MODEL

The hybrid quantum lattice consists of a one-dimensional array of cavity quantum electrodynamics (QED) systems, each comprising a single-mode cavity interacting with a single two-level system (TLS), as shown schematically in Fig. 1. In addition to the light-matter interaction, the TLSs interact directly with their nearest neighbors. An *activation qubit* (emitter) is placed at the first site of the hybrid quantum lattice, and its primary role is to inject a single excitation into the cavity-QED array. The activation qubit is directly coupled to the TLS of the first cavity QED unit, located at site $j = 2$. The hybrid quantum lattice supports the propagation of three types of single excitations: photon, polariton and spin wave.

The system Hamiltonian consists of three contributions, $H = H_{\rm A}+H_{\rm JC}+H_{\rm I}$. Here, $H_{\rm A}$ describes the activation qubit and its interaction with the cavity-QED array. $H_{\rm JC}$ denotes the interaction between each cavity mode

* maritza.ahumada@usm.cl

† guillermo.romero@usach.cl

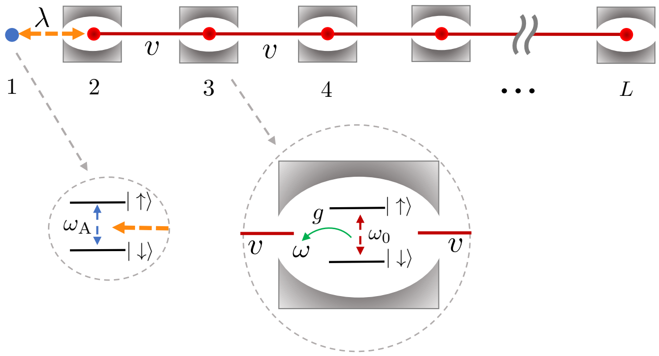

FIG. 1. Schematic representation of hybrid quantum lattice. The blue dot represents the activation qubit (left inset) with frequency $\omega_{\rm A}$, which is coupled to the TLS of the first QED unit with coupling strength λ (orange segmented arrow). The right inset shows a cavity QED unit, in which a single cavity mode interacts with a TLS. The TLSs interact with their nearest neighbors with coupling strength v (red solid line).

and its corresponding TLS via the Jaynes-Cummings model [58–60]. $H_{\rm I}$ accounts for the nearest-neighbor interaction between the TLSs. These terms are given by

$$H_{\rm A} = \hbar\omega_{\rm A}\,\hat{\sigma}_1^+\hat{\sigma}_1^- + \hbar\lambda\left(\hat{\sigma}_1^+\hat{\sigma}_2^- + \hat{\sigma}_1^-\hat{\sigma}_2^+\right)\,, \tag{1}$$

$$H_{\rm JC} = \sum_{j=2}^{L}\hbar\left[\omega\,\hat{a}_j^\dagger\hat{a}_j + \omega_0\,\hat{\sigma}_j^+\hat{\sigma}_j^- + g\left(\hat{\sigma}_j^+\hat{a}_j + \hat{\sigma}_j^-\hat{a}_j^\dagger\right)\right]\,, \tag{2}$$

$$H_{\rm I} = \sum_{j=2}^{L-1}\hbar v\left(\hat{\sigma}_j^+\hat{\sigma}_{j+1}^- + \hat{\sigma}_j^-\hat{\sigma}_{j+1}^+\right)\,, \tag{3}$$

where $\hat{a}_j^\dagger$ ($\hat{a}_j$) is the creation (annihilation) operator of a single bosonic excitation in the j-th cavity with frequency ω, and $\hat{\sigma}_j^+$ and $\hat{\sigma}_j^-$ are the raising and lowering operators of the j-th TLS in the eigenbasis $\{|\uparrow_j\rangle, |\downarrow_j\rangle\}$. Additionally, $\omega_{\rm A}$ denotes the frequency of the activation qubit, ω_0 the transition frequency of the TLSs in the cavity-QED array, g the light–matter coupling strength, λ the coupling strength between the activation qubit and the TLS in the first cavity-QED, and v the coupling strength between nearest-neighbor TLSs.

To analyze the propagation of different types of single excitations, it is convenient to rewrite the full Hamiltonian in the basis of hybrid light–matter states, i.e., the upper (+) and lower (−) polaritonic basis states

$$|n,\alpha\rangle_j = \gamma_{n\alpha}|\downarrow,n\rangle_j + \rho_{n\alpha}|\uparrow,n-1\rangle_j\,, \tag{4}$$

where $\alpha = \pm$ denotes the polaritonic branches. The coefficients are defined by

$$\rho_{n+} = \cos\left(\frac{\theta_n}{2}\right),\quad \gamma_{n+} = \sin\left(\frac{\theta_n}{2}\right),$$
$$\rho_{n-} = -\gamma_{n+},\quad \rho_{n+} = \gamma_{n-}\,, \tag{5}$$

and the mixing angle θ_n is given by $\tan(\theta_n) = 2g\sqrt{n}/\Delta$ with $\Delta = \omega_0 - \omega$ as the detuning.

The energy eigenvalues associated with these eigenstates are

$$E_n^\alpha/\hbar = n\omega + \frac{\Delta}{2} \pm \frac{\Delta}{2}\sqrt{1+\frac{4ng^2}{\Delta^2}}\,. \tag{6}$$

The polaritonic creation operator at the jth site is $P_j^{\dagger(n,\alpha)} = |n,\alpha\rangle_j\langle 0,-|$, where $|\downarrow,0\rangle = |0,-\rangle$ is the ground state and the unphysical state $|0,+\rangle = |\varnothing\rangle$ is a null vector. The previous determines the values of $\gamma_{0-} = 1$ and $\gamma_{0+} = \rho_{0\alpha} = 0$.

The terms of the Hamiltonian written in the polaritonic basis are

$$\begin{aligned} H_{\rm A} = {} & \hbar\omega_{\rm A}\,\hat{\sigma}_1^+\hat{\sigma}_1^- + \\ & \hbar\lambda\hat{\sigma}_1^+\sum_{n=0}^{\infty}\sum_{\alpha,\beta=\pm}\rho_{n\alpha}\gamma_{n-1\beta}\hat{P}_2^{\dagger(n-1,\beta)}\hat{P}_2^{(n,\alpha)} + \\ & \hbar\lambda\hat{\sigma}_1^-\sum_{n=0}^{\infty}\sum_{\alpha,\beta=\pm}\rho_{n\alpha}\gamma_{n-1\beta}\hat{P}_2^{\dagger(n,\alpha)}\hat{P}_2^{(n-1,\beta)}, \end{aligned} \tag{7}$$

$$H_{\rm JC} = \hbar\sum_{j=2}^{L}\sum_{n=0}^{\infty}\sum_{\alpha=\pm}E_n^\alpha\hat{P}_j^{\dagger(n,\alpha)}\hat{P}_j^{(n,\alpha)}, \tag{8}$$

$$\begin{aligned} H_{\rm I} = \hbar v\sum_{j=2}^{L-1}\sum_{n,m=1}^{\infty}\sum_{\substack{\alpha,\alpha'=\pm\\ \beta,\beta'=\pm}} & \Big[t_n^{\alpha\beta}t_m^{\alpha'\beta'}\hat{P}_j^{\dagger(n,\alpha)}\hat{P}_j^{(n-1,\beta)} \\ & \hat{P}_{j+1}^{\dagger(m-1,\beta')}\hat{P}_{j+1}^{(m,\alpha')} + \text{h.c.}\Big], \end{aligned} \tag{9}$$

where $t_n^{\alpha\beta} = \rho_{n\alpha}\gamma_{n-1\beta}$. See Appendix A for further details.

III. MULTIPLE EXCITATIONS PROPAGATION

In this section, we expose the propagation mechanism of different types of excitations, namely, polaritons, spin waves, and photons, within a unified platform: the hybrid quantum lattice. The propagation dynamics of each excitation type depend on tuning key parameters: the light–matter coupling strength, the activation qubit frequency, and the coupling between neighboring TLSs. As will be shown later, by tuning these parameters and suppressing the excitation propagation through the upper polaritonic branch, we can select the type of information carrier propagating in the system. We focus on two distinct cases of light-matter interaction: the resonant and dispersive regimes. In the resonant regime, where $\Delta = \omega_0 - \omega = 0$, polaritons dominate the dynamics. In contrast, in the dispersive regime, where $|\Delta| \gg g$, the single photon and spin-wave excitation become the dominant information carriers.

We perform numerical simulations using the TEBD algorithm [54–56]. We numerically approximate the evolution operator using the Suzuki-Trotter decomposition [61]

$$e^{-i\tau(F+G)} \approx \prod_{l=1}^{k} e^{-i\tau(c_l F)}\, e^{-i\tau(d_l G)} + O(\tau^{n+1}), \quad (10)$$

where F and G contain the sum of the Hamiltonian terms for the even and odd bonds [54], respectively. In particular, we use the second-order ($n = 2$) approximant, where the expansion parameters of Eq. (10) are $k = 2$, $c_1 = 1/2$, $d_1 = 1$, $c_2 = 1/2$, $d_2 = 0$. Besides, we consider a time-step $\tau = 10^{-3}v^{-1}$ for spin and polariton propagation, and $\tau = 5 \times 10^{-3}v^{-1}$ for photon propagation, the total system size of $L = 26$ sites, the accessible number states in each cavity is $n_{\max} = 2$, and the maximum bond dimension is $\chi_{\max} = 4$. Within the simulated time, the latter ensures a truncation error $\epsilon_{\text{trunc}} \lesssim 10^{-8}$, see Appendix C.

We use an initial condition that enables the activation of the hybrid quantum lattice. The activation qubit can undergo a transition from $|\uparrow_1\rangle$ to $|\downarrow_1\rangle$, thereby transferring a single excitation. This initial state is given by

$$|\Psi_0\rangle = |\uparrow_1\rangle \otimes |\downarrow, 0\rangle_2 \otimes |\downarrow, 0\rangle_3 \otimes \cdots \otimes |\downarrow, 0\rangle_L \,. \quad (11)$$

In the following, we present the dynamics of each type of single excitation and give details on the conditions under which they emerge.

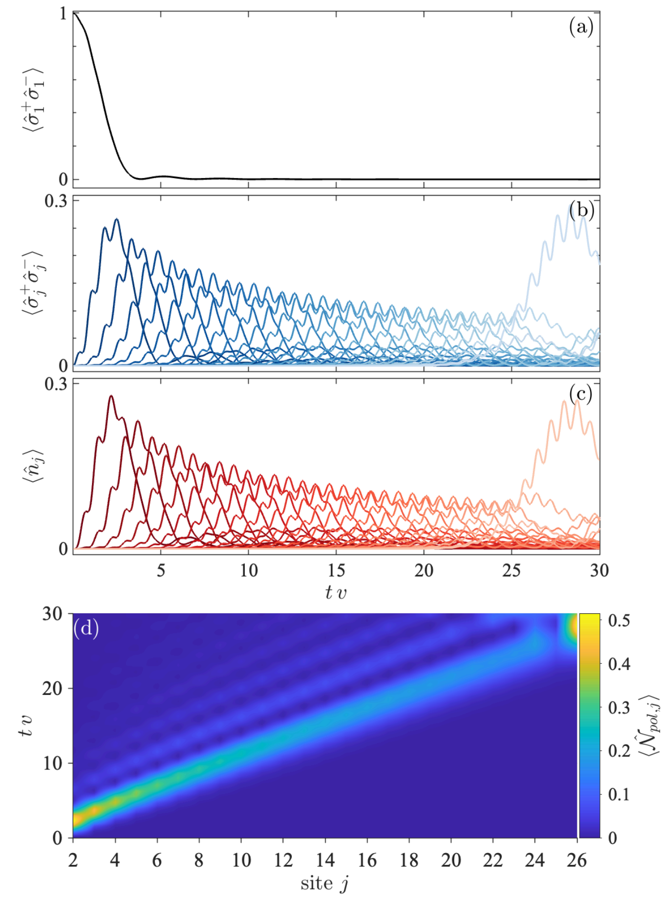

FIG. 2. Polariton-wave propagation: (a) Time evolution of the average excitation number in the activation qubit. (b) Time evolution of the average excitation number in the jth TLS of the cavity-QED array, for $2 \leq j \leq 26$. (c) Average photon number as a function of time. (d) Average polariton number as a function of time and the site index j. The parameters are $\Delta = 0$ with $\omega = \omega_0 = 1$, $v = 0.01\,\omega$, $g = 4\,v$, $\omega_A = \omega_{pol} = \omega - g$, $\lambda = -v/\sqrt{2}$, $\tau = 10^{-3}v^{-1}$, and $L = 26$.

A. Resonant regime: polariton propagation

Hereafter, and for the sake of simplicity, we will consider the lower polaritonic branch for a single polariton propagating along the network. The latter is possible if three conditions are fulfilled.

1. The propagation through the upper polaritonic branch is suppressed if $g \gg |v|/4$. The derivation of this condition is provided in Appendix A. Appendix B provides a numerical analysis confirming the suppression of propagation in the upper polaritonic branch under this condition.

2. The frequency of the activation qubit must be resonant with the transition frequency of the lower polaritonic branch, i.e., $\omega_A = \omega - g$. The energy levels in the lower polaritonic branch are given in Eq. (12)

$$E_n^-/\hbar = n\omega + \frac{\Delta}{2} - \frac{1}{2}\sqrt{\Delta^2 + 4ng^2}\,. \quad (12)$$

In the resonant regime, $\Delta = 0$, and considering a single excitation, $n = 1$, Eq. (12) reduces to

$$E_1^-/\hbar = \omega - g = \omega_{pol}\,. \quad (13)$$

3. The effective coupling between the activation qubit and the first polariton must match the effective coupling between two nearest-neighbor polaritons. This conditions leads to $\lambda = -v/\sqrt{2}$.

To determine the third condition, we focus on the Hamiltonian H_I in the representation of the polaritonic basis, Eq. (9), which accounts for the polariton hopping between nearest-neighbour sites. In the case of a single excitation propagating through the lower polaritonic branch, the indexes correspond to $n = 1$, $\alpha = \beta = -$, $m = 1$, $\alpha' = \beta' = -$, and the effective coupling between polariton nearest-neighbour reads

$$\tilde v = v\, t_1^{--}\, t_1^{--} = v\,(\rho_{1-}\,\gamma_{0-})^2 = v\,(\rho_{1-})^2\,. \quad (14)$$

Let us focus on the Hamiltonian H_A in Eq. (7). From this expression, the effective coupling between the activation qubit and the first polariton is given by

$$\tilde\lambda = \lambda\,\rho_{1-}\,\gamma_{0-} = \lambda\,\rho_{1-}\,, \quad (15)$$

Both effective coupling matches, resulting

$$\tilde{\lambda} = \tilde{v} \Rightarrow \lambda = v\,\rho_{1-}\,, \tag{16}$$

where using Eqs. (5)

$$\rho_{1-} = -\sin\left(\frac{\theta_1}{2}\right), \quad \text{with} \quad \tan(\theta_1) = \frac{2g}{\Delta}\,. \tag{17}$$

The match impedance condition Eqs. (16) is valid for any Δ. In the particular case of the resonant regime, $\Delta = 0$ and $\tan(\theta_1)$ diverge at $\theta_1 = \pi/2$, resulting in $\rho_{1-} = -1/\sqrt{2}$, and the condition reduces to $\lambda = -v/\sqrt{2}$.

Tuning the lattice parameters to satisfy the three previously described conditions enables the propagation of a single polariton through the hybrid quantum lattice. Figure 2 shows the mechanism of single-excitation generation, its release, and subsequent polariton propagation. Figure 2(a) displays the behavior of the activation qubit, where the average excitation number $\langle \hat{\sigma}_1^+ \hat{\sigma}_1^- \rangle = 1$ at $t = 0$, and eventually decays to 0, injecting a single excitation into the hybrid system. Once released, the excitation propagates to the right as a single polariton. Figures 2(b) and 2(c) show the average excitation number of the jth TLS and the average photon number in each cavity, respectively. Since the polariton number operator is defined as $\langle \hat{\mathcal{N}}_{pol,j} \rangle = \langle \hat{\sigma}_j^+ \hat{\sigma}_j^- \rangle + \langle \hat{n}_j \rangle$, these two figures separately depict the respective contributions of spin and photon components to the polariton dynamics. The overall polariton propagation through the lattice is presented in Fig. 2(d), where the average polariton number $\langle \hat{\mathcal{N}}_{pol,j} \rangle$ is plotted as a function of time and site index j. The polaritonic excitation appears as a dispersive pulse, with a decreasing amplitude and increasing width over time.

B. Dispersive regime: photon propagation

In the dispersive regime ($|\Delta| \gg g$), single-photon propagation through the cavity array is possible even when the average excitation number of the jth TLS remains approximately zero. In this regime, the photon transport is mediated by the hybrid light–matter excitations, namely the polaritons. For photon propagation to occur, the following conditions must be satisfied:

1. The condition $g \gg |v/4|$ ensures the suppression of propagation through the upper polaritonic branch.

2. The frequency of the activation qubit must be resonant with the transition frequency of the lower polaritonic branch. In the dispersive regime, the condition is now $\omega_A = \omega - g^2/\Delta$. From Eq. (12), the energy levels in the lower polaritonic branch reads

$$E_n^-/\hbar = n\omega + \frac{\Delta}{2} - \frac{\Delta}{2}\sqrt{1+\chi(n)}\,, \quad \chi(n) = \frac{4g^2 n}{\Delta^2}. \tag{18}$$

In the dispersive regime, $|\Delta| \gg g$ and the quantity $\chi(n) \ll 1$, allowing to expand the square root in the third term of Eq. (18) as a Taylor series around $\chi(n)$. This yields,

$$E_n^-/\hbar \simeq \omega + \frac{\Delta}{2} - \frac{\Delta}{2}\left(1 + \frac{\chi(n)}{2}\right) = \left(\omega - \frac{g^2}{\Delta}\right) n\,. \tag{19}$$

Thus, considering a single excitation $n = 1$, the energy Eq. (19) reduces to

$$E_1^-/\hbar = \omega - \frac{g^2}{\Delta} \tag{20}$$

3. The effective coupling between the activation qubit and the first polariton must match the effective coupling between two nearest-neighbor polaritons, $\lambda = v\,\rho_{1,-}$ [see Eqs. (16) and (17)].

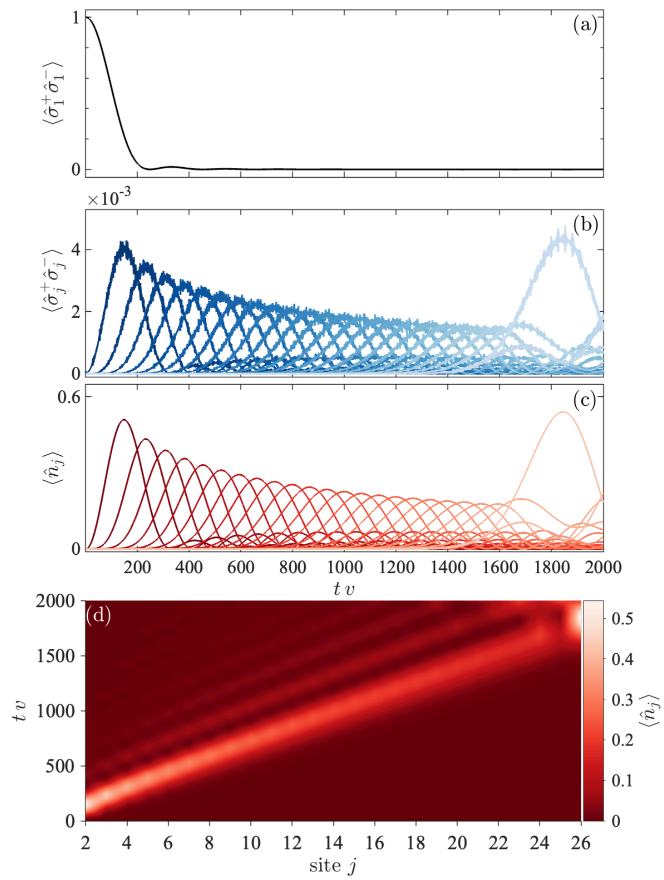

FIG. 3. Photon-wave propagation: (a) Time evolution of the average excitation number in the activation qubit. (b) Time evolution of the average excitation number in the jth TLS of the cavity-QED array, for $2 \leq j \leq 26$. (c) Average photon number as a function of time. (d) Average photon number as a function of time and the site index j. The parameters are $\omega = 10$, $\omega_0 = 1$, $\Delta = \omega_0 - \omega$, $g = 0.08\,\omega$, $\omega_A = \omega - g^2/\Delta$, $v = 0.05\,\omega$, $\lambda = -v\,\sin(\theta_1/2)$ with $\theta_1 = \arctan(2g/\Delta)$, $\tau = 5\times 10^{-3} v^{-1}$, and $L = 26$.

Single-photon propagation in the hybrid system is illustrated in Fig. 3. By tuning the system parameters

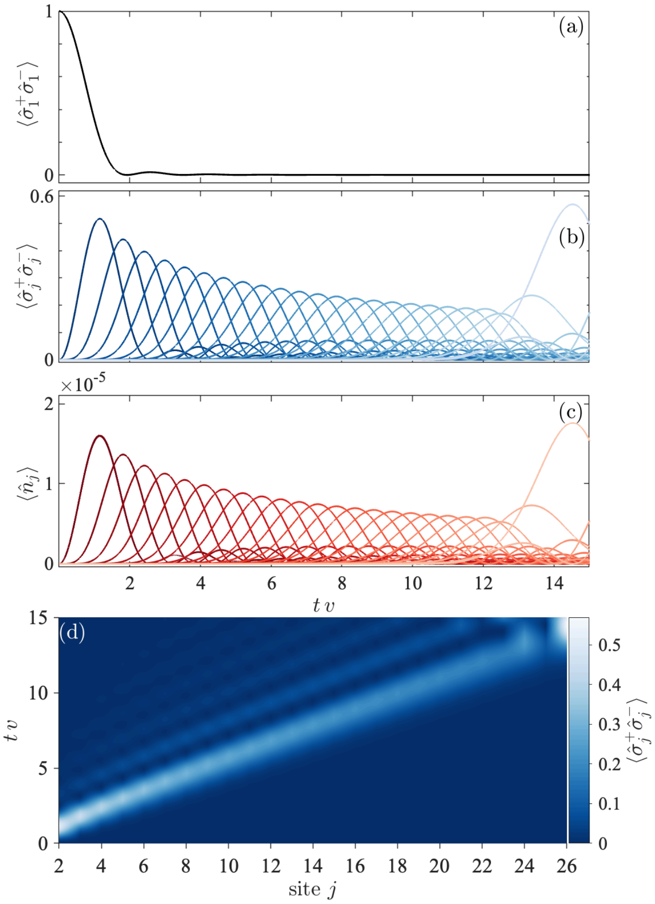

FIG. 4. Spin-wave propagation: (a) Time evolution of the average excitation number in the activation qubit. (b) Time evolution of the average excitation number in the jth TLS of the cavity-QED array, for $2 \leq j \leq 26$. (c) Average photon number as a function of time. (d) Average excitation number in the jth TLS as a function of time and the site index j. The parameters are $\omega = 1$, $\omega_0 = 10$, $\Delta = \omega_0 - \omega$, $\omega_A = \omega_0$, $g = 0.05\,\omega$, $v = 0.02\,\omega$, $\lambda = v$, $\tau = 10^{-3}v^{-1}$, and $L = 26$.

to satisfy the last three conditions associated with this case, photon-like excitations dominate the transport dynamics. As in the polariton case, the excitation originates from the activation qubit and is released into the system. Once injected, it propagates to the right, now as a single photon, through the cavity array, even though the cavities are not directly coupled to each other. Figures 3(b) and 3(c) show the average excitation number of the jth TLS and the average photon number in each cavity, respectively. In this case, the values of $\langle\hat{\sigma}_j^+\hat{\sigma}_j^-\rangle$ in Fig. 3(b) remain close to zero, while in Fig. 3(c) the photon number reveals a propagating excitation pulse through the cavities. Figure 3(d) provides a broader view of the photon propagation dynamics across the hybrid lattice.

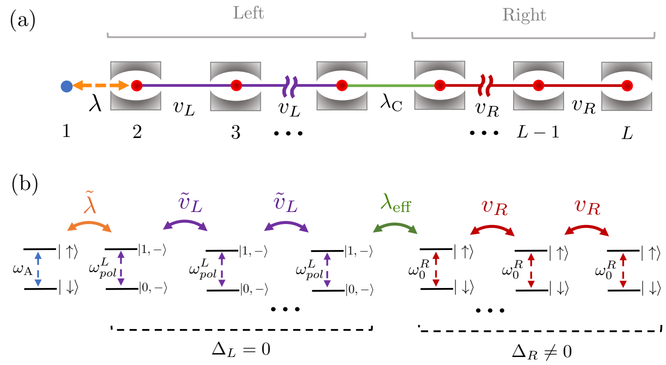

FIG. 5. (a) Schematic of the hybrid quantum lattice divided into two sections (left and right), each characterized by distinct parameter sets. (b) Schematic representation of the effective energy levels, effective coupling, and impedance-matching interface (green curve arrow), enabling an excitation swap of the type polariton → spin-wave can occur. The polariton transition frequencies and effective couplings between nearest-neighbour polaritons are indicated with purple arrows, while those corresponding to the spin-wave are shown in red. The orange arrow indicates the effective coupling between the activation qubit and the first polariton.

C. Dispersive regime: Spin wave propagation

In the dispersive regime ($|\Delta| \gg g$), a second case of interest is the propagation of spin-wave excitations. This regime allows for the transport of energy through the TLS sublattice, while the photonic component remains largely unexcited. The following conditions must be satisfied:

1. The condition $g \gg |v/4|$ ensures the suppression of propagation through the upper polaritonic branch.
2. The frequency of the activation qubit must be resonant with the transition frequency of the TLSs in the cavity-QED array, i.e., $\omega_A = \omega_0$.
3. The coupling between the activation qubit and the TLS in the first cavity unit must match the coupling strength between neighboring TLSs, i.e., $\lambda = v$.

Spin-wave propagation under these conditions is illustrated in Fig. 4. Once released, the excitation propagates through the lattice via the TLS sublattice, forming a spin-wave [see Fig. 4(b)]. In this case, the average photon number in each cavity remains negligible across all sites [see Fig. 4(c)]. Figure 4(d) provides a global view of the excitation dynamics, showing the transport of the spin-wave through the hybrid lattice.

IV. EXCITATION SWAP

The hybrid quantum lattice allows controlled switching between excitation types through parameter tuning. As

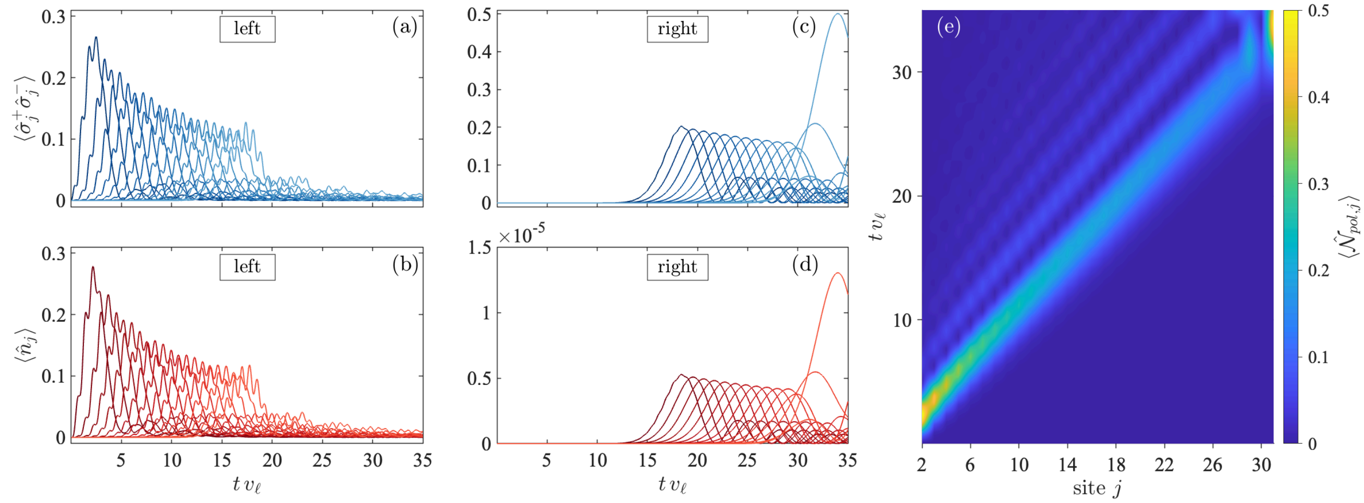

FIG. 6. Dynamic excitation swap, polariton $\to$ spin-wave: Average excitation number of the jth TLS and the average photon number as functions of time for the left section (ℓ), shown in panels (a) and (b), and for the right section (r), shown in panels (c) and (d), respectively. (e) Average polariton number as a function of time and the site index j (with $2 \leq j \leq 31$). The parameters in the left section are $\omega_\ell = \omega_0^\ell = 1$, $\Delta_\ell = \omega_0^\ell - \omega_\ell = 0$, $v_\ell = 0.05\,\omega_\ell$, $g_\ell = 4v_\ell$, $\omega_{\rm A} = \omega_{pol}^\ell = \omega_\ell - g_\ell$, $\lambda = -v_\ell/\sqrt{2}$. In the right section, the parameter are $\omega_0^r = \omega_{pol}^\ell$, $\omega_r = 50\,\omega_0^r$, $\Delta_r = \omega_0^r - \omega_r$, $g_r = g_\ell$, $\theta_1 = \arctan(2g_r/\Delta_r)$, $v_r = v_\ell/2$. Additional lattice parameters are $\tau = 10^{-3} v_\ell^{-1}$, $n_{\max} = 2$, and $L = 31$.

shown in the previous sections, depending on the regime (resonant or dispersive) and the specific conditions satisfied, the same injected excitation can propagate as a polariton, a photon, or a spin wave. This tunability enables a dynamic excitation swap, where the type of information carrier changes during propagation.

To illustrate this mechanism, we divide the hybrid lattice into two sections, left and right, as shown in Fig. 5(a). All lattice parameters are labeled with ℓ and r to indicate their respective sector. The excitation is injected into the left side via the activation qubit and propagates from left to right. The parameters are chosen such that the excitation propagates as one type on the left side and swaps to another type on the right side. The connection between the two regions is modeled by a coupling $\lambda_{\rm C}$, which acts analogously to an impedance-matching interface. Figure 5(b) shows a schematic representation of the effective energy levels, effective couplings, and the effective impedance-matching coupling. This configuration enables an excitation swap of the type polariton (left section) $\to$ spin-wave (right section).

The activation qubit injects the excitation, which propagates as a polariton in the left section provided that the conditions detailed in Section III A are satisfied. The interface coupling $\lambda_{\rm C}$ is dressed by the polaritonic state on the left side, yielding the following effective impedance-matching coupling:

$$\lambda_{\rm eff} = \rho_{1-}^\ell \lambda_{\rm C}\,. \tag{21}$$

Note that $\lambda_{\rm C}$ is not dressed by the right side, since the selected excitation propagating in that region is a spin wave. For the excitation to be fully transmitted across the interface, the reflection on the left side must be minimized to near zero. This requires that the effective hopping of the polariton match the effective impedance-matching coupling, i.e., $\tilde{v}_\ell = \lambda_{\rm eff}$, where $\tilde{v}_\ell = v_\ell(\rho_{1-}^\ell)^2$ [see Eq. 14]. The last expression implies the following

$$\lambda_{\rm C} = v_\ell\, \rho_{1-}^\ell\,. \tag{22}$$

Additionally, the effective impedance-matching coupling must also match the coupling between TLSs in the right section, leading to:

$$\lambda_{\rm eff} = v_r\,. \tag{23}$$

Substituting the Eqs. (21) and (22) into Eq. (23), and using $\rho_{1-}^\ell = -1/\sqrt{2}$ [see Eqs. 17 with $\Delta = 0$], we obtain a relation between the coupling constants of nearest-neighbor TLSs in the left and right sections of the hybrid lattice

$$v_r = \frac{v_\ell}{2}\,. \tag{24}$$

Figure 6 illustrates the dynamic excitation swap from a polariton to a spin wave. This figure presents the average excitation number of the jth TLS, $\langle \hat{\sigma}_j^+ \hat{\sigma}_j^- \rangle$ (upper row), and the average photon number, $\langle \hat{n}_j \rangle$ (lower row), as functions of time for each j-th cavity unit. Figures 6(a) and 6(b) show the dynamics of these two components of the average polariton number, $\langle \hat{\mathcal{N}}_{pol,j} \rangle$, on the left side of the lattice ($2 \leq j \leq 15$). In this region, both components contribute equally to the propagation of the excitation pulse. As the pulse reaches the interface and enters the right section, both photon and TLS contributions in the left region diminish nearly to zero, indicating efficient transmission with no observable reflection. Figures 6(c) and 6(d) display the corresponding dynamics in the right section ($16 \leq j \leq 31$). The excitation continues to propagate as a spin wave, as evidenced in Fig.6(c), while the photon number remains negligible, as shown in Fig.6(d). Figure 6(e) provides a complete view of the excitation dynamics across the entire system, showing the average polariton number $\langle \hat{\mathcal{N}}_{pol,j} \rangle$ as a function of time and site index. This global perspective confirms the efficient transfer of excitation from the polariton on the left to the spin wave on the right, with negligible reflection at the interface. Additionally, the propagation velocity remains unchanged across the two regions, as evidenced by the continuous linear slope of the excitation pulse.

It is noteworthy that the excitation swap mechanism can also be realized in alternative hybrid lattice configurations. In particular, we consider a setup where the activation qubit is disconnected, and the system is initially prepared in a single polariton state localized at the center of the lattice ($j = (L+1)/2$ with L odd). In this configuration, the lattice parameters are chosen such that the excitation propagates as a polariton to the left and as a spin wave to the right. The two pulses propagate in opposite directions, from the center toward the lattice boundaries, while conserving the total number of excitations, a single excitation. The impedance-matching condition between the two sections, λ_{C} is given by Eq. (22), and the coupling between TLSs in the right section, v_r, is determined by Eq. (24).

V. CONCLUSION

In summary, our study demonstrates that a one-dimensional hybrid quantum lattice model, combining cavity QED units with direct spin-spin interactions, enables controlled propagation and swapping of quantum excitations, namely, polaritons, spin waves, and photons. By adjusting system parameters to satisfy impedance and resonance conditions, we show how these excitations can be selectively guided or coherently swapped, with polaritons serving as the interface between photonic and spin-wave domains. For photon transport, we find that polaritonic states mediate single-excitation propagation, with negligible contribution from atomic excitations. This architecture provides a versatile platform for quantum links, where distant emitters can efficiently interact through polaritonic, spin-wave, or photonic networks, enabling robust quantum state transfer, hybrid information processing, and reconfigurable quantum networks. Future work should explore higher-excitation extensions, disorder effects, non-Markovian quantum links communicating emitters, and experimental implementations to advance these concepts for scalable quantum technologies further.

ACKNOWLEDGMENTS

M. A. acknowledges financial support from Postdoctoral FONDECYT Grant No. 3240443. We also thank the support from Dicyt USACH under grant 042331RH_Ayudante, and Centro de Investigación Asociativa ANID CIA 250002.

Appendix A: Polaritonic basis

The eigenstates of the Jaynes-Cummings model define the upper (+) and lower (−) polaritonic basis, which is used to write the Hamiltonian of our model to analyze the effective couplings to propagate the different excitations. A compact way to write the basis is to use the following notation

$$|n, \alpha\rangle_j = \gamma_{n\alpha} |\downarrow, n\rangle_j + \rho_{n\alpha} |\uparrow, n-1\rangle_j \tag{A1}$$

with energies

$$E_n^\alpha/\hbar = n\omega + \frac{\Delta}{2} \pm \frac{\Delta}{2}\sqrt{1 + \frac{4g^2 n}{\Delta^2}} \tag{A2}$$

where the polaritonic branches are indicated by the index $\alpha = \pm$, n refers to the number of polaritons and the coefficients on the basis are defined as $\rho_{n+} = \cos(\frac{\theta_n}{2})$, $\gamma_{n+} = \sin(\frac{\theta_n}{2})$, $\rho_{n-} = -\gamma_{n+}$, $\rho_{n+} = \gamma_{n-}$, θ_n is defined by $\tan(\theta_n) = 2g\sqrt{n}/\Delta$, and $\Delta = \omega_0 - \omega$ is the detuning parameter.

The ground state is identified as $|\downarrow, 0\rangle = |0, -\rangle$ and the non-physical state $|0, +\rangle = |\mathbf{\emptyset}\rangle$ is a ket with all entries equal to zero. The previous determines the values of $\gamma_{0-} = 1$ and $\gamma_{0+} = \rho_{0\alpha} = 0$. Also, the polaritonic creation operator can be introduced for the jth site as $P_j^{\dagger(n,\alpha)} = |n, \alpha\rangle_j \langle 0, -|$.

The Jaynes-Cummings model, written in the polaritonic basis reads

$$H_{\mathrm{JC}} = \sum_{j=1}^{L} \sum_{n=0}^{\infty} \sum_{\alpha=\pm} E_n^\alpha P_j^{\dagger(n,\alpha)} P_j^{(n,\alpha)}. \tag{A3}$$

Also, the equations for H_A and H_I contain terms of the raising and lowering operators. We change the representation of these terms using the completeness relation of the polaritonic basis, $\mathbf{I}_j = \sum_{n=0}^{\infty} \sum_{\alpha=\pm} P_j^{\dagger(n,\alpha)} P_j^{(n,\alpha)}$, dropping the site index j for practicality in the meantime, such that,

$$\begin{aligned} \mathbf{I}\,\hat{\sigma}^+ \mathbf{I} &= \sum_{n,m=0}^{\infty} \sum_{\alpha,\beta=\pm} P^{\dagger(n,\alpha)} P^{(n,\alpha)} \hat{\sigma}^+ P^{\dagger(m,\beta)} P^{(m,\beta)} \\ &= \sum_{n,m=0}^{\infty} \sum_{\alpha,\beta=\pm} \langle n, \alpha | \hat{\sigma}^+ | m, \beta \rangle P^{\dagger(n,\alpha)} P^{(m,\beta)} \end{aligned} \tag{A4}$$

and the matrix element is $\langle n,\alpha|\hat{\sigma}^+|m,\beta\rangle = \big(\gamma_{n\alpha}\langle\downarrow,n| + \rho_{n\alpha}\langle\uparrow,n-1|\big)\hat{\sigma}^+\big(\gamma_{m\beta}|\downarrow,m\rangle + \rho_{m\beta}|\uparrow,m-1\rangle\big)$. Considering the operator $\hat{\sigma}^+$ acts on the TLS and the orthogonality between the states we obtain

$$\langle n,\alpha|\ \hat{\sigma}^+\ |m,\beta\rangle = \rho_{n\alpha}\gamma_{m\beta}\ \delta_{n-1,m}.$$

Here, the Kronecker delta is chosen such that $m = n-1$

$$\mathbf{I}\ \hat{\sigma}^+\mathbf{I} = \sum_{n=1}^{\infty}\sum_{\alpha,\beta=\pm}\rho_{n\alpha}\gamma_{n-1\beta}P^{\dagger(n,\alpha)}P^{(n-1,\beta)}$$

and taking into account $\hat{\sigma}^- = (\hat{\sigma}^+)^\dagger$ we have

$$\hat{\sigma}_j^+\hat{\sigma}_{j+1}^- = \sum_{n,m=1}^{\infty}\sum_{\substack{\alpha,\alpha'=\pm\\ \beta,\beta'=\pm}}\big(\rho_{n\alpha}\gamma_{n-1\beta}\rho_{m\alpha'}\gamma_{m-1\beta'}P_j^{\dagger(n,\alpha)}\times P_j^{(n-1,\beta)}P_{j+1}^{\dagger(m-1,\beta')}P_{j+1}^{(m,\alpha')}\big)$$

and accordingly, their complex conjugate. Considering the previous, with abbreviated notation $t_n^{\alpha\beta} = \rho_{n\alpha}\gamma_{n-1\beta}$, the H_I Hamiltonian on the polaritonic basis is

$$H_I = \hbar v\sum_{j}^{L-1}\sum_{n,m=1}^{\infty}\sum_{\substack{\alpha,\alpha'=\pm\\ \beta,\beta'=\pm}}\big[t_n^{\alpha\beta}t_m^{\alpha'\beta'}P_j^{\dagger(n,\alpha)}P_j^{(n-1,\beta)}\times P_{j+1}^{\dagger(m-1,\beta')}P_{j+1}^{(m,\alpha')} + \text{h.c}\big] \tag{A5}$$

Now we move to the interaction picture. We compute $\mathcal{H_I} = U^\dagger VU$ with the evolution operator being $U(t) = \exp(-\frac{i}{\hbar}\sum_j^L H_{\mathrm{JC}_j}t)$. Since the operators of different sites commute, we have local evolution operators for each site as $U(t) = \prod_j^L U_j(t)$ with

$$U_j(t) = \exp\left(-\frac{i}{\hbar}\sum_{n=1}^{\infty}\sum_{\alpha=\pm}F_n^\alpha(t)P_j^{\dagger(n,\alpha)}P_j^{(n,\alpha)}\right) = \sum_{n=1}^{\infty}\sum_{\alpha=\pm}\mathrm{e}^{-\frac{i}{\hbar}F_n^\alpha(t)}P_j^{\dagger(n,\alpha)}P_j^{(n,\alpha)}$$

where $F_n^\alpha(t) = E_n^\alpha t$. As a result of the previous, we only need to compute two terms: I) $U_j^\dagger(t)P_j^{\dagger(n,\alpha)}P_j^{(n-1,\beta)}U_j(t)$ and II) $U_{j+1}^\dagger(t)P_{j+1}^{\dagger(m-1,\beta')}P_{j+1}^{(m,\alpha')}U_{j+1}(t)$. Without loss of generality, we calculate the terms I and II for a general index site $j = l$, and we highlight that the polaritonic branch indexes and the number of polaritons are independent for every operator of these terms. Consequently, for the local evolution operators, we introduce the indexes η and μ for the number of excitations and ζ and ξ for the polaritonic branches.

$$\text{I) } U^\dagger P^{\dagger(n,\alpha)}P^{(n-1,\beta)}U = \sum_{\eta,\mu=1}^{\infty}\sum_{\zeta,\xi=\pm}\mathrm{e}^{\frac{i}{\hbar}F_\eta^\zeta}\mathrm{e}^{-\frac{i}{\hbar}F_\mu^\xi}P^{\dagger(\eta,\zeta)}P^{(\eta,\zeta)}P^{\dagger(n,\alpha)}P^{(n-1,\beta)}P^{\dagger(\mu,\xi)}P^{(\mu,\xi)} = \sum_{\eta,\mu=1}^{\infty}\sum_{\zeta,\xi=\pm}\mathrm{e}^{\frac{i}{\hbar}(F_\eta^\zeta - F_\mu^\xi)}\delta_{\eta,n}\delta_{\zeta,\alpha}\delta_{n-1,\mu}\delta_{\beta,\xi}\ |\eta,\zeta\rangle\ \langle\mu,\xi|$$

The last line of the equation above is obtained by considering the explicit form of the polaritonic operators in terms of the states and the orthogonality of the basis. Similarly, the second term reads

$$\text{II) } U^\dagger P^{\dagger(m-1,\beta')}P^{(m,\alpha')}U = \sum_{\eta',\mu'=1}^{\infty}\sum_{\zeta',\xi'=\pm}\mathrm{e}^{\frac{i}{\hbar}(F_{\eta'}^{\zeta'} - F_{\mu'}^{\xi'})}\times\delta_{\eta',m-1}\delta_{\zeta',\beta'}\delta_{m,\mu'}\delta_{\alpha',\xi'}\ |\eta',\zeta'\rangle\ \langle\mu',\xi'|$$

Solving the deltas such that all is in terms of $n,\ m,\ \alpha\ (\alpha')$ and $\beta\ (\beta')$ and transforming the states back into the polaritonic operator form, we obtain $\mathcal{H_I} = U^\dagger VU$. In addition, for the sake of notation space, we define $\mathcal{T}_{nm}^{\alpha\beta\alpha'\beta'} = vt_n^{\alpha\beta}t_m^{\alpha'\beta'}$

$$\mathcal{H_I} = \hbar\sum_{j=1}^{L-1}\left(\sum_{\substack{n,\\ m}=1}^{\infty}\sum_{\substack{\alpha,\alpha'=\pm\\ \beta,\beta'=\pm}}\mathcal{T}_{nm}^{\alpha\beta\alpha'\beta'}\mathrm{e}^{\frac{i}{\hbar}(F_n^\alpha - F_{n-1}^\beta + F_{m-1}^{\beta'} - F_m^{\alpha'})}\times P_j^{\dagger(n,\alpha)}P_j^{(n-1,\beta)}P_{j+1}^{\dagger(m-1,\beta')}P_{j+1}^{(m,\alpha')} + h.c\right) \tag{A6}$$

We choose to propagate polaritons through the lower branch; therefore, propagation through the upper polaritonic branch must be suppressed. Considering two general contiguous sites of the chain in which there is a polariton, $\ldots|1,-\rangle_l\,|0,-\rangle_{l+1}\ldots$, we expect that the propagation of the polariton will be $\ldots|0,-\rangle_l\,|1,-\rangle_{l+1}\ldots$ instead of $\ldots|0,-\rangle_l\,|1,+\rangle_{l+1}\ldots$. The hermitian conjugate part in the Hamiltonian of equation (A6) leads to the term $|0,-\rangle_l\,|1,\alpha'\rangle_{l+1}$. The indices for propagation through the upper branch correspond to $n = m = 1$, $\alpha = \beta' = \beta = -$, and $\alpha' = +$. The latter implies two things. In the first place, for the energy values in the exponential term of equation (A6) we have $\exp\big(-\frac{i}{\hbar}[E_1^- - E_1^+]t\big) = \exp\big(\frac{2i}{\hbar}\big[\sqrt{\Delta^2/4+g^2}\big]t\big)$. Since we are in the resonant regime we obtain $\exp\big(\frac{2i}{\hbar}gt\big)$. In second place $\mathcal{T}_{11}^{--+-} = vt_1^{--}t_1^{+-} = v(\rho_{1-}\gamma_{0-}\rho_{1+}\gamma_{0-}) = -\frac{v}{2}\sin\theta_1$. Remembering the definition $\tan\frac{2g\sqrt{n}}{\Delta} = \frac{\sin\theta_n}{\cos\theta_n}$, and since $\Delta = 0$, then $\tan\theta_1 \to \infty$. For this reason, we choose $\theta_1 = (2k+1)\pi/2; k \in \mathbb{Z}$. Due to the rotating-wave approximation, we obtain the condition to suppress the fast oscillating terms as $2g \gg \mathcal{T}_{11}^{--+-}$, and restrain the propagation of polaritons through the upper branch.

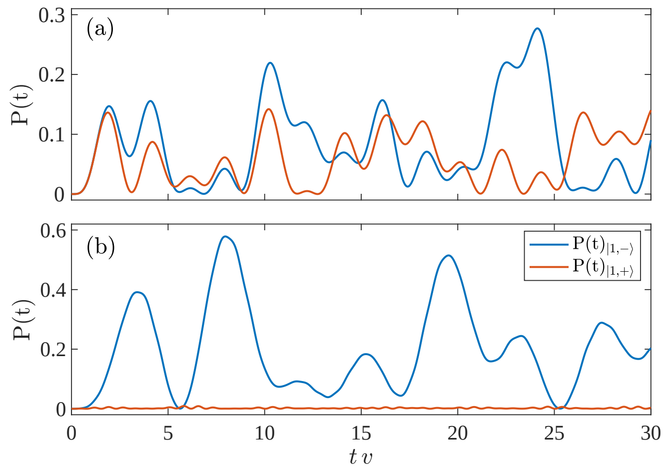

FIG. B1. Polaritonic branch populations as a function of time in units of v, (a) for $g = v/4$ and (b) $g = 4v$, satisfying the condition of Eq. (A7).

Finally, considering the previous and the fact that the amplitude of the interacting term is what matters, the condition is written as

$$g \gg \frac{|v|}{4} \tag{A7}$$

Appendix B: Polaritonic branch populations

Here, we present numerical results for the population of the upper and lower polaritonic branches. We are interested in verifying the condition $g \gg |v|/4$ where the upper polaritonic branch is suppressed and the lower polaritonic branch is populated by activation qubit frequency condition $\omega_A = \omega - g$. We numerically solve the time-dependent Schrödinger equation using exact diagonalization. We thus consider a reduced system of $L = 4$ sites, restricting the photonic Hilbert space to at most $n_{\max} = 2$ photons per cavity. This choice is justified by our observation that only the $n = 1$ subspace is appreciably populated, with higher Fock states contributing negligibly to the total. In figure B1, we show the polaritonic branch populations for two cases: when $g = v/4$ and $g = 4v$, for the cavity in the site $j = 3$. In the first case, we observe that the population of the upper polaritonic branch is comparable to that of the lower branch, reaching approximately 10%. This suggests that the polaritonic excitation propagates through both branches simultaneously. In the second case, only the lower polaritonic branch is significantly populated, thus confirming the regime $g \gg \frac{|v|}{4}$, where the dynamics is dominated by a single polaritonic branch.

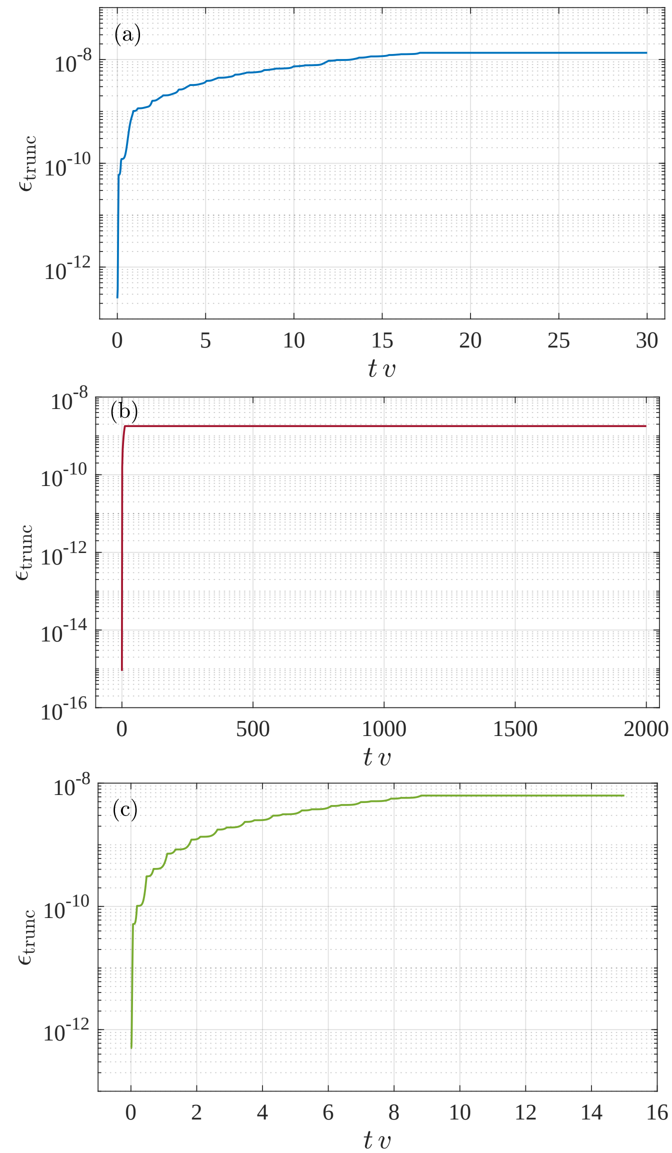

FIG. C1. Polariton: TEBD-truncation error as a function of time for (a) polariton, (b) photon, and (c) spin-wave propagation. The vertical axis scale is logarithmic using base 10.

Appendix C: Truncation error

In the TEBD algorithm, a two-site wave function's split and truncate procedure in a mixed canonical form involves the singular value decomposition (SDV) of a 4-rank multidimensional array. The SVD allows us to compute $\mathrm{norm}_{\rm old} = \sqrt{\sum_a \lambda_a^2}$ where λ_a are the Schmidt coefficients. Then, we proceed with the truncation by keeping the Schmidt coefficients larger than a given threshold ϵ_0, which we fix to $\epsilon_0 = 10^{-6}$ in our algorithm. The new bond dimension of the updated matrix product state (MPS) is computed as $\min(\chi_{\max}, N_{\rm kept})$ where $N_{\rm kept}$ is the number of kept singular values, and $\chi_{\max}$ is the maximum bond dimension of the MPS which we fix to $\chi_{\max} = 4$. Introducing the threshold value ϵ_0 allows an adaptive bond dimension along the quantum lattice, thus saving computational time. Once the truncation has been done, we compute $\text{norm}_{\text{new}} = \sqrt{\sum_{a=1}^{N_{\text{kept}}} \lambda_a^2}$ and $1 - 2\epsilon_n$, where $\epsilon_n = 1 - (\text{norm}_{\text{new}}/\text{norm}_{\text{old}})^2$. The described procedure is done each time a two-body unitary is applied following the Suzuki-Trotter decomposition [61] of the evolution operator, and the quantity $1 - 2\epsilon_n$ is saved in a vector. The total truncation error is computed as $\epsilon_{\text{trunc}} = 1 - \prod_n (1 - 2\epsilon_n)$ [62].

Figures C1(a), C1(b), and C1(c) show the truncation error as a function of time of polariton, photon, and spin-wave propagation, respectively. In each case, we see that $\epsilon_{\text{trunc}} \lesssim 10^{-8}$. The negligible truncation error over time is explained since a single excitation propagates along the lattice.

[1] H. J. Kimble, The quantum internet, Nature **453**, 1023 (2008).
[2] S. Wehner, D. Elkouss, and R. Hanson, Quantum internet: A vision for the road ahead, Science **362**, 10.1126/science.aam9288 (2018).
[3] A. A. Houck, H. E. Türeci, and J. Koch, On-chip quantum simulation with superconducting circuits, Nature Physics **8**, 292 (2012).
[4] I. M. Georgescu, S. Ashhab, and F. Nori, Quantum simulation, Reviews of Modern Physics **86**, 153 (2014).
[5] J. Feist and F. J. Garcia-Vidal, Extraordinary exciton conductance induced by strong coupling, Physical Review Letters **114**, 196402 (2015).
[6] B. X. K. Chng, E. Mondal, and P. Huo, Quantum dynamics simulations of exciton polariton transport, Nano Letters **25**, 1234 (2025).
[7] J. I. Cirac, P. Zoller, H. J. Kimble, and H. Mabuchi, Quantum State Transfer and Entanglement Distribution among Distant Nodes in a Quantum Network, Phys. Rev. Lett. **78**, 3221 (1997).
[8] M. Christandl, N. Datta, A. Ekert, and A. J. Landahl, Perfect State Transfer in Quantum Spin Networks, Phys. Rev. Lett. **92**, 187902 (2004).
[9] T. Shi, Y. Li, Z. Song, and C.-P. Sun, Quantum-state transfer via the ferromagnetic chain in a spatially modulated field, Phys. Rev. A **71**, 032309 (2005).
[10] D. Burgarth and S. Bose, Perfect quantum state transfer with randomly coupled quantum chains, New J. Phys. **7**, 135 (2005).
[11] D. Burgarth and S. Bose, Conclusive and arbitrarily perfect quantum-state transfer using parallel spin-chain channels, Phys. Rev. A **71**, 052315 (2005).
[12] A. Perez-Leija, R. Keil, A. Kay, H. Moya-Cessa, S. Nolte, L.-C. Kwek, B. M. Rodríguez-Lara, A. Szameit, and D. N. Christodoulides, Coherent quantum transport in photonic lattices, Phys. Rev. A **87**, 012309 (2013).
[13] J. Ghosh, Emulating quantum state transfer through a spin-1 chain on a one-dimensional lattice of superconducting qutrits, Phys. Rev. A **90**, 062318 (2014).
[14] *Quantum State Transfer and Network Engineering* (Springer, Berlin, Germany, 2014).
[15] S. Ashhab, Quantum state transfer in a disordered one-dimensional lattice, Phys. Rev. A **92**, 062305 (2015).
[16] L.-Y. Cheng, L.-N. Zheng, R. Wu, H.-F. Wang, and S. Zhang, Change-over switch for quantum states transfer with topological channels in a circuit-QED lattice, Chin. Phys. B **31**, 020305 (2022).
[17] G. F. Peñas, R. Puebla, and J. J. García-Ripoll, Improving quantum state transfer: correcting non-Markovian and distortion effects, Quantum Sci. Technol. **8**, 045026 (2023).
[18] G. F. Peñas, R. Puebla, and J. J. García-Ripoll, Multiplexed quantum state transfer in waveguides, Phys. Rev. Res. **6**, 033294 (2024).
[19] J. I. Cirac, A. K. Ekert, S. F. Huelga, and C. Macchiavello, Distributed quantum computation over noisy channels, Phys. Rev. A **59**, 4249 (1999).
[20] A. Serafini, S. Mancini, and S. Bose, Distributed Quantum Computation via Optical Fibers, Phys. Rev. Lett. **96**, 010503 (2006).
[21] Z.-q. Yin and F.-l. Li, Multiatom and resonant interaction scheme for quantum state transfer and logical gates between two remote cavities via an optical fiber, Phys. Rev. A **75**, 012324 (2007).
[22] C. J. Axline, L. D. Burkhart, W. Pfaff, M. Zhang, K. Chou, P. Campagne-Ibarcq, P. Reinhold, L. Frunzio, S. M. Girvin, L. Jiang, M. H. Devoret, and R. J. Schoelkopf, On-demand quantum state transfer and entanglement between remote microwave cavity memories, Nat. Phys. **14**, 705 (2018).
[23] P. Kurpiers, P. Magnard, T. Walter, B. Royer, M. Pechal, J. Heinsoo, Y. Salathé, A. Akin, S. Storz, J.-C. Besse, S. Gasparinetti, A. Blais, and A. Wallraff, Deterministic quantum state transfer and remote entanglement using microwave photons, Nature **558**, 264 (2018).
[24] N. Leung, Y. Lu, S. Chakram, R. K. Naik, N. Earnest, R. Ma, K. Jacobs, A. N. Cleland, and D. I. Schuster, Deterministic bidirectional communication and remote entanglement generation between superconducting qubits, npj Quantum Inf. **5**, 1 (2019).
[25] G. F. Peñas, R. Puebla, T. Ramos, P. Rabl, and J. J. García-Ripoll, Universal Deterministic Quantum Operations in Microwave Quantum Links, Phys. Rev. Appl. **17**, 054038 (2022).
[26] C. Ciuti and I. Carusotto, Quantum fluid effects and parametric instabilities in microcavities, Phys. Status Solidi B **242**, 2224 (2005).
[27] I. Carusotto and C. Ciuti, Quantum fluids of light, Reviews of Modern Physics **85**, 299 (2013).
[28] S. Bose, Quantum communication through an unmodulated spin chain, Physical Review Letters **91**, 207901 (2003).
[29] R. Ohira, S. Kume, H. Takahashi, and K. Toyoda, Polariton blockade in the Jaynes–Cummings–Hubbard model with trapped ions, Quantum Sci. Technol. **6**, 024015 (2021).
[30] S. Muralidharan and K. Toyoda, Site-dependent control of polaritons in the Jaynes–Cummings–Hubbard model with trapped ions, Appl. Phys. B **129**, 1 (2023).
[31] X. Li, Y. Ma, J. Han, T. Chen, Y. Xu, W. Cai, H. Wang,

Y. P. Song, Z.-Y. Xue, Z.-q. Yin, and L. Sun, Perfect Quantum State Transfer in a Superconducting Qubit Chain with Parametrically Tunable Couplings, Phys. Rev. Appl. **10**, 054009 (2018).

[32] L. Xiang, J. Chen, Z. Zhu, Z. Song, Z. Bao, X. Zhu, F. Jin, K. Wang, S. Xu, Y. Zou, H. Li, Z. Wang, C. Song, A. Yue, J. Partridge, Q. Guo, R. Mondaini, H. Wang, and R. T. Scalettar, Enhanced quantum state transfer by circumventing quantum chaotic behavior, Nat. Commun. **15**, 1 (2024).

[33] F. A. Roy, J. H. Romeiro, L. Koch, I. Tsitsilin, J. Schirk, N. J. Glaser, N. Bruckmoser, M. Singh, F. X. Haslbeck, G. B. P. Huber, G. Krylov, A. Marx, F. Pfeiffer, C. M. F. Schneider, C. Schweizer, F. Wallner, D. Bunch, L. Richard, L. Södergren, K. Liegener, M. Werninghaus, and S. Filipp, Parity-dependent state transfer for direct entanglement generation, Nat. Commun. **16**, 1 (2025).

[34] A. D. Greentree, C. Tahan, J. H. Cole, and L. C. L. Hollenberg, Quantum phase transitions of light, Nat. Phys. **2**, 856 (2006).

[35] M. J. Hartmann, F. G. S. L. Brandão, and M. B. Plenio, Strongly interacting polaritons in coupled arrays of cavities, Nat. Phys. **2**, 849 (2006).

[36] D. G. Angelakis, M. F. Santos, and S. Bose, Photon-blockade-induced Mott transitions and XY spin models in coupled cavity arrays, Phys. Rev. A **76**, 031805 (2007).

[37] J. Koch and K. Le Hur, Superfluid–Mott-insulator transition of light in the Jaynes-Cummings lattice, Phys. Rev. A **80**, 023811 (2009).

[38] M. I. Makin, J. H. Cole, C. D. Hill, A. D. Greentree, and L. C. L. Hollenberg, Time evolution of the one-dimensional Jaynes-Cummings-Hubbard Hamiltonian, Phys. Rev. A **80**, 043842 (2009).

[39] C. Nietner and A. Pelster, Ginzburg-Landau theory for the Jaynes-Cummings-Hubbard model, Phys. Rev. A **85**, 043831 (2012).

[40] A. L. C. Hayward, A. M. Martin, and A. D. Greentree, Fractional Quantum Hall Physics in Jaynes-Cummings-Hubbard Lattices, Phys. Rev. Lett. **108**, 223602 (2012).

[41] B. Bujnowski, J. K. Corso, A. L. C. Hayward, J. H. Cole, and A. M. Martin, Supersolid phases of light in extended Jaynes-Cummings-Hubbard systems, Phys. Rev. A **90**, 043801 (2014).

[42] J. Xue, K. Seo, L. Tian, and T. Xiang, Quantum phase transition in a multiconnected Jaynes-Cummings lattice, Phys. Rev. B **96**, 174502 (2017).

[43] J. Figueroa, J. Rogan, J. A. Valdivia, M. Kiwi, G. Romero, and F. Torres, Nucleation of superfluid-light domains in a quenched dynamics, Sci. Rep. **8**, 1 (2018).

[44] S. B. Prasad and A. M. Martin, Effective Three-Body Interactions in Jaynes-Cummings-Hubbard Systems, Sci. Rep. **8**, 1 (2018).

[45] R. Peña, F. Torres, and G. Romero, Dynamical dimerization phase in Jaynes–Cummings lattices, New J. Phys. **22**, 033034 (2020).

[46] Q. Li, J.-L. Ma, T. Huang, L. Tan, H.-Q. Gu, and W.-M. Liu, Quantum quench dynamics of the Jaynes-Cummings-Hubbard model with weak nearest-neighbor hopping, Europhys. Lett. **134**, 20007 (2021).

[47] A. Norambuena, F. Torres, M. Di Ventra, and R. Coto, Polariton-based quantum memristors, Phys. Rev. Appl. **17**, 024056 (2022).

[48] J.-L. Ma, Q. Li, and L. Tan, Ergodic and nonergodic phases in a one-dimensional clean Jaynes-Cummings-Hubbard system with detuning, Phys. Rev. B **105**, 165432 (2022).

[49] B.-W. Li, Q.-X. Mei, Y.-K. Wu, M.-L. Cai, Y. Wang, L. Yao, Z.-C. Zhou, and L.-M. Duan, Observation of Non-Markovian Spin Dynamics in a Jaynes-Cummings-Hubbard Model Using a Trapped-Ion Quantum Simulator, Phys. Rev. Lett. **129**, 140501 (2022).

[50] M. Tudorovskaya and D. Muñoz Ramo, Quantum computing simulation of a mixed spin-boson Hamiltonian and its performance for a cavity quantum electrodynamics problem, Phys. Rev. A **109**, 032612 (2024).

[51] A. Karnieli, S. Tsesses, R. Yu, N. Rivera, A. Arie, I. Kaminer, and S. Fan, Universal and ultrafast quantum computation based on free-electron-polariton blockade, PRX Quantum **5**, 010339 (2024).

[52] E. Baum, A. Broman, T. Clarke, N. C. Costa, J. Mucciaccio, A. Yue, Y. Zhang, V. Norman, J. Patton, M. Radulaski, and R. T. Scalettar, Effect of emitters on quantum state transfer in coupled cavity arrays, Phys. Rev. B **105**, 195429 (2022).

[53] A. Yue, R. Mondaini, Q. Guo, and R. T. Scalettar, Quantum state transfer in interacting multiple-excitation systems, Phys. Rev. B **110**, 195410 (2024).

[54] G. Vidal, Efficient simulation of one-dimensional quantum many-body systems, Physical Review Letters **93**, 040502 (2004).

[55] A. J. Daley, C. Kollath, U. Schollwöck, and G. Vidal, Time-dependent density-matrix renormalization-group using adaptive effective hilbert spaces, Journal of Statistical Mechanics: Theory and Experiment **2004**, P04005 (2004).

[56] U. Schollwöck, The density-matrix renormalization group in the age of matrix product states, Annals of Physics **326**, 96 (2011).

[57] C. Barahona-Pascual, H. Jiang, A. C. Santos, and J. J. García-Ripoll, Time-delayed collective dynamics in waveguide qed and bosonic quantum networks (2025), arXiv:2505.02642 [quant-ph].

[58] E. T. Jaynes and F. W. Cummings, Comparison of quantum and semiclassical radiation theories with application to the beam maser, Proc. IEEE **51**, 89 (1963).

[59] J. Larson, T. Mavrogordatos, T. Mavrogordatos, S. Parkins, S. Parkins, and A. Vidiella-Barranco, The Jaynes–Cummings model: 60 years and still counting, J. Opt. Soc. Am. B, JOSAB **41**, JCM1 (2024).

[60] J. Larson and T. Mavrogordatos, *The Jaynes–Cummings Model and its Descendants (Second Edition) – Modern research directions* (IOP Publishing, Bristol, England, UK, 2024).

[61] N. Hatano and M. Suzuki, Finding exponential product formulas of higher orders, in *Quantum Annealing and Other Optimization Methods*, edited by A. Das and B. K. Chakrabarti (Springer Berlin Heidelberg, Berlin, Heidelberg, 2005) pp. 37–68.

[62] J. Hauschild, J. Unfried, S. Anand, B. Andrews, M. Bintz, U. Borla, S. Divic, M. Drescher, J. Geiger, M. Hefel, K. Hémery, W. Kadow, J. Kemp, N. Kirchner, V. S. Liu, G. Möller, D. Parker, M. Rader, A. Romen, S. Scalet, L. Schoonderwoerd, M. Schulz, T. Soejima, P. Thoma, Y. Wu, P. Zechmann, L. Zweng, R. S. K. Mong, M. P. Zaletel, and F. Pollmann, Tensor network Python (TeNPy) version 1, SciPost Phys. Codebases , 41 (2024).